Journal for Extragalactic Astronomy Projects, 1, 1.
Preprint typeset using LaTeX style emulateapj v. 11/10/09

EXAMINING SUPERNOVA REMNANT/INTERSTELLAR MEDIUM INTERACTIONS IN THE LARGE MAGELLANIC CLOUD WITH WISE

S. De Pascuale and C. DeRoo
Department of Physics and Astronomy, University of Iowa, Iowa City, IA, 52242
Journal for Extragalactic Astronomy Projects, 1, 1.

ABSTRACT

The energy input, chemical enrichment, and shock turbulance associated with supernova remnants (SNR) make them influential objects in the dynamics and evolution of the interstellar medium (ISM). Characterizing the ISM/SNR interaction requires observations across multiple frequency regimes, with infrared (IR) being the most essential to trace heated ISM material interacting with SNR shocks. In this spirit, we employ archival *ROSAT* observations and data from the CSIRO Parkes Radio Telescope, as analyzed by Williams et al. 1999 and Filipoviċ et al. 1998 respectively, as well as new observations from the Wide-Field Infrared Survey Explorer (WISE) operating in the infrared (3.4, 4.6, 12, and 22 μm) to examine 45 known SNRs in the Large Magellanic Cloud (LMC). We characterize the SNR sources using their observed 22 μm WISE band morphology and calculate total IR fluxes from the heated ISM material contained within the SNR. We also use the WISE point-source catalog to search for YSOs proximal to LMC SNRs to search for evidence of SNR shock-triggered star formation.

We find that remnants characterized by strong, roughly spherical 22 μm emission (D-class herein) are young, dusty remnants which are more X-ray luminous than other LMC SNR counterparts. In addition, we conclude that for the majority of LMC remnants, polycyclic aromatic hydrocarbons (PAHs) and small grain dust has been dissociated by SNR-associated shocks. We also observe evidence for large grain dust destruction over timescales of $\sim$ 4000 years. Finally, we find no evidence for SNR shock-triggered star formation in the LMC, and conclude that this is likely not an important process for forming stars in the LMC.

Subject headings: supernova remnants — ISM: dust — Large Magellanic Cloud

1. INTRODUCTION

Supernova remnants (SNRs) are the astrophysical remains of a supernova (SN) explosion. SNe are caused by either a massive giant branch star undergoing rapid gravitational collapse through the cessation of efficient fusion in its core (a core-collapse SN) or a white dwarf entering a thermonuclear reaction after accreting mass above the Chandrasekhar limit (Type Ia SN). In either case, an outward propagating shock causes a large fraction of the stellar envelope to be shed, forming a shell of supersonic ejecta which expands outward into the interstellar medium (ISM). This ejecta mixes with the surrounding ISM during the expansion phase of the SNR, heating the surrounding gas and dust and enriching the ISM with stellar fusion products.

Because of the prodigious energy deposition and shock turbulance associated with SNe, these events and the subsequent development of their remnants play an essential role in the dynamics of the ISM. Furthermore, SNRs are responsible for distributing the majority of the metals into the ISM (Fukugita & Peebles 2004), and hence are one of the primary sources of chemical enrichment in the universe. Finally, it has been suggested (Vanhala & Cameron 1998) that SNRs may influence star formation through the interaction of the blast wave with self-gravitating molecular cloud cores. Hence, SNRs represent an important class of objects whose development and dynamics impact the evolution of the ISM and star formation on a galactic scale.

In order to generalize about the impact of SNRs on such large scales, however, it is necessary to have a statistically sufficient number of resolved remnants for study. In the Milky Way, line-of-sight absorption impedes the construction of a complete and unbiased survey sample across multiple wavebands. While there are at least 274 identified SNR within the Milky Way (Green 2009), selection effects such as the obstruction of interstellar dust, particularly along lines of sight within the galactic disk, prevent observations at all wavebands.

In contrast, the line of sight to the Large Magellanic Cloud (LMC) has comparatively low absorption, as the LMC (at $b \sim 33°$) is outside the "zone of avoidance" and only moderately inclined ($i = 35°$; van der Marel & Cioni 2001). This comparatively low obscuration towards and in the LMC yields a sample of SNRs that is both relatively complete and of adequate size (45 confirmed SNR candidates to date; Desai et al 2010, hereafter D2010). Furthermore, the LMC is relatively nearby ($\sim$ 50 kpc; di Benedetto 2008), meaning that the bulk of target SNRs can be resolved in the X-ray (which traces the superheated, shocked ejecta) and the infrared (which traces ISM density and shock heating processes) by current observatories. With the completion of the recent Wide-Field Infrared Survey Explorer (WISE) All-Sky Survey, capable of providing observations of LMC remnants in four IR wavebands, 3.4, 4.6, 12, and 22 μm, the time is ripe to undertake a multi-frequency study of this SNR population.

Surveying SNRs in the LMC also provides a unique opportunity in that the LMC ISM has an average metallicity 0.2 dex lower than the local Galactic ISM, and thus is underenriched (Russell & Dopita 1992). Hence, studying SNRs in the LMC can be likened to studying their impact in a cosmologically younger Milky Way.

1.1. *Dynamic Evolution of SNRs*

In order to better understand the ISM/SNR interaction, it is necessary to characterize the expansion dynamics of an aging remnant. The dynamical evolution of SNRs can be broken into four evolutionary phases and is governed by the ratio of the ejecta mass (M_{ejecta}) to the mass of the swept-up ISM (M_{ISM}). At the outset, the SN blast wave travels at a nearly constant velocity of order 10^4 km/s as it expands into the surrounding medium, sweeping up nearby dust and gas and heating it to temperatures of $\sim 10^6 - 10^7$ K. This phase, in which $M_{ISM} << M_{ejecta}$, is the "free-expansion" phase and can last for several hundred years depending on the density of the local medium (Chevalier 1977).

When the swept-up ISM mass is roughly equal to the ejecta mass ($M_{ejecta} \sim M_{ISM}$), the remnant enters the adiabatic expansion or Sedov-Taylor phase. X-ray line emission and thermal brehmstrahlung can be observed during this phase; this emission traces shocked, dense material in the interior of the blast wave. However, as radiative cooling processes are relatively inefficient at these high temperatures, the total energy of the remnant during this phase is essentially conserved. As a result of the acculumation of more ISM mass, the expansion rate slows, being governed by the initial energy of the SN and the local ISM density. Self-similar analytical models of the remnant's expansion during this phase can be constructed using simplifying geometries (Sedov 1959).

As the mass of the swept-up ISM comes to dominate the remnant's total mass ($M_{ISM} >> M_{ejecta}$), the remnant enters the pressure-driven "snowplow" phase of its dynamic evolution. At lower temperatures, radiative cooling processes become much more efficient as atoms are no longer fully ionized. Finally, the remnant enters a radiative phase for which the remnant is sufficiently cool ($\sim 10^5$ K) to permit UV/optical line emission. The shocks dissipate into the surrounding medium, heating the local environment and thoroughly mixing the ejecta material with the ISM. Significant local turbulance can accelerate this dynamical phase, which dominates the total lifetime of the remnant ($\sim 10^5$ years). Nevertheless, the lifespan of an SNR is short in comparison with the timescale of galactic evolution.

1.2. *IR emission from SNRs*

As the shocks and turbulance associated with the SNR propagate outward, it is expected that the surrounding dust and gas will be heated and thermally radiate in the infrared (IR). Predominant emission mechanisms in the mid-IR that might be expected for SNR include atomic lines, rotational/vibrational modes of molecular hydrogen, excitation of the polycyclic aromatic hydrocarbon (PAH) bands, IR synchrotron, and thermal continuum emission from dust grains (Reach et al. 2006). However, these mid-IR features are certainly not observed in all remnants, and their presence (or absence) can be used as a diagnostic of the ISM/SNR interaction and the mixing of ejecta and ISM material.

For instance, PAHs are thought to be dissociated by strong shocks of velocities higher than 100 km s^{-1}, and have lifetimes of $\leq 10^3$ years in low density, hot media (Micelotta et al. 2010a, b). This implies that PAHs ought to be destroyed when interacting with a nascent, expansion-phase SNR. Shock destruction has been observationally confirmed for four Balmer-dominated Type Ia remnants in the LMC (Borkowski et al. 2006), while PAH emission has been observed in several Galactic SNR whose shock velocities are decreased due to the dense surrounding environment (Andersen et al. 2011). However, this PAH diagnostic for the velocity of the expansion shock does not appear to be foolproof: PAH features have been observed in the young LMC remnant N132D (Tappe et al. 2006). More work is need to understand the presence or absence of PAH features in the context of interacting ISM/SNRs.

With optical Hα observations, it is possible to determine the contribution of roto-vibrational H_2 lines to the observed IR emission, and additional optical observations can further constrain the contributions of other atomic line emission processes (Maggi et al. 2012). Broadband observations in the mid-/far-IR can then be used to infer the temperature of dust grains within and nearby the expanding SNR. In particular, the broad wavelength range made available by the *Spitzer Space Telescope* enabled IR surveys of LMC and Galactic SNRs capable of estimating dust temperatures, remnant ages and swept-up ISM mass when convolved with appropriate dust population models (e.g. Borkowski et al. 2006, Reach et al. 2006).

1.3. *SNRs and Star Formation*

SNRs are often found within or near star formation regions (SFRs). This is not unexpected: for core-collapse SNe, their massive progenitors are more likely to form in stellar clusters or large OB associations, and their short main sequence lifetimes (10^7 years) allow the possibility of multiple SN generations over the lifetime of an SFR. However, it is has been suggested that the shocks resulting from a SN blast wave may be able to trigger the collapse of nearby molecular cloud cores, thus creating an "SN feedback loop" within these SFRs. Observational evidence for shock-triggered star formation is plentiful, and has been observed in systems involving stellar winds (e.g. Thompson et al. 1998, Chen et al. 1993). Particularly striking for the purpose at hand is evidence of triggered star formation in the stellar association CMa R1, which lies on the edge of an old SNR (Herbst & Assousa 1977).

Theoretical calculations also suggest that shocks may be able to induce collapse in self-gravitating molecular cloud cores through ram pressure interaction, though the end result (compression or destruction) is highly sensitive to the magnitude of the shock velocity. Rapidly moving shocks ($v_{shock} \sim 1000$ km s^{-1}) shred self-gravitating molecular clouds due to Rayleigh-Taylor and Kelvin-Helmholtz instabilities resulting from the shock front/molecular cloud interaction (e.g. Stone & Norman 1992, Klein, McKee & Colella 1994). On the other hand, slow-moving shocks ($v_{shock} \leq 25$–45 km s^{-1}) interacting with self-gravitating molecular cloud cores may be able to induce gravitational collapse. Boss (1995) found that these mild shock waves can compress self-gravitating molecular clouds to the point of collapse on shorter timescales than plasma instabilities can tear the cloud apart, and that high post-shock temperatures were considerably more efficient in compressing the cloud. Additionally, it was found that up to 40% of the shock wave material could be incorporated into the protostellar object. Foster & Boss (1996) examined the collapse of molecular cloud cores interacting with stellar ejecta, such as that from stellar winds or SN blast waves, and concluded that the critical shock momentum which induces collapse scales with the mass of the cloud and the local sound speed. They also find that for shock velocities greater than ~ 100 km s^{-1}, molecular cloud core collapse will be prevented due to the destruction of cooling agents within the cloud.

1.4. *Purpose of the Present Work*

In order to obtain a comprehensive picture of SNR/ISM interaction, multi-wavelength observations are necessary to probe material at a wide variety of temperatures and densities. In this paper, we examine IR observations of 45 known SNRs in the LMC taken with WISE. We categorize these diffuse sources based on their 22 μm (W4 band) morphologies, and calculate flux magnitudes by integrating over their optically-identified extents. We combine this with archival data from *ROSAT* and the Commonwealth Scientific and Industrial Research Organisation (CSIRO) Parkes Radio Telescope, as analyzed by Williams et al. 1999 (hereafter W1999) and Filipovic̀ et al. 1998 (hereafter F1998) respectively, to examine the X-ray morphology, emission intensity of the X-ray plasma, and the dynamic age of the SNR. In addition, we search the WISE point-source catalog for nearby young stellar objects (YSOs) in order to examine evidence for SNR shock-triggered star formation. These data are described in §2, §3 includes our analysis of the multi-wavelength data, and §4 will discuss the implications of our findings.

2. OBSERVATIONS

2.1. *Source Catalog*

For this paper, we consider a catalog of the 45 known SNRs in the LMC as compiled by D2010 (Table 2). This source catalog was initially compiled using observations by the *Einstein* Observatory (Mathewson et al. 1983, 1984, 1985), and has had additional members identified via *ROSAT* X-ray observations (Chu et al. 1993, 1995, 1997; Smith et al. 1994) or by high [S II]/Hα ratios (Points et al. 2004). D2010 defines the location and extents of the LMC SNRs based on observations from the Magellanic Cloud Emission Line Survey (MCELS; [O III], Hα, [S II]), and reports the center, the major axis length, and minor axis length of an ellipse containing the SNR. To verify the reliability of this catalog, we calculate the [S II]/Hα ratio of the total flux within the catalog-specified source regions. The majority of our sources (40 of 45 total) have ratios > 0.4, meeting the criterion for optical identification as an SNR, and no source has a ratio [S II]/H$\alpha \leq 0.1$, as would be expected for an HII region (Fesen et al. 1985). Hence, our catalog is assumed to contain only objects that are SNRs.

2.2. *Infrared Observations*

In order to trace the interaction of these SNRs with ISM material, this study makes use of archival WISE image data. WISE observed in four wavelength bands: 3.4 (W1), 4.6 (W2), 12 (W3) and 22 μm (W4). These filters correspond to various emission components of interstellar dust; the 3.4 and 12 μm bands observe PAH emission features, the 4.6 μm band measures thermal continuum from small dust grains, and the 22 μm band includes contributions from both the stochastic heating of small grains and the Wien tail of thermal emission from large dust grains (Wright et al. 2010).

NASA/IPAC's Infrared Science Archive (IRSA) provides access to co-added single-frame images taken from WISE, which were combined to form digital mosaic of the entire sky at a 5σ sensitivity of 0.08, 0.11, 1, and 6 mJy in the 3.4, 4.6, 12, and 22 μm bands respectively. We used this service to obtain $10'$ square cut-outs from the WISE All-Sky Release[1], as well as a catalog of WISE-detected point sources within a cone of radius $10'$ from the WISE Catalog Search[2], both centered around the position of each source.

2.3. *Calculating WISE Band Magnitudes*

Unlike the progenitor star that is considered to be a discrete point source, the daughter SNR is quite diffuse spatially and covers multiple WISE pixels at the LMC distance. Comparing the total WISE band brightness of the sources, therefore, requires integrating over the extent of each SNR and converting the sum to a flux measurement for the sources. This procedure is performed following the explanatory supplement to the WISE All-Sky Data Release Products, [3] which we briefly discuss here.

First, a circular region is defined for each SNR, which is centered on the catalog SNR location and has diameter equal to the major axis of the ellipse reported by D2010. Next, an integration scheme is applied to sum the pixels within this region and obtain a total flux value, F_{tot}. The instrument flux F_i, or the source flux in instrumental units, is then measured by subtracting the background contribution for the total number of pixels, N_A, in the selected aperture where $\bar{B}$ is a robust determination of the local background level per pixel.

$$F_i = f_{apcor}(F_{tot} - N_A \bar{B}). \tag{1}$$

In order to estimate the local background $\bar{B}$, a circular background region was visually identified for each $10'$ cut-out. This background region was selected to have the lowest total source flux within the cut-out (i.e. contain the dimmest part of the image). The average pixel value within the background region was taken to be $\bar{B}$, while the standard deviation of these values suffices as an estimate of the average pixel uncertainty, σ_{src}.

Given limitations of the instrument, the WISE band aperture point-spread function (PSF) is accounted for by a factor, f_{apcor}, in (1); however, no color correction or extinction correction is included because of the unknown intrinsic energy distribution of the source. Lastly, source fluxes F_{src} are calculated in W cm^{-}2 by use of the following equation:

$$F_{src} \text{W cm}^{-2} = \lambda \frac{F^0_\lambda}{10^{m_{zp}/2.5}} F_i \tag{2}$$

[1] http://irsa.ipac.caltech.edu/applications/wise/
[2] http://irsa.ipac.caltech.edu/cgi-bin/Gator/nph-dd
[3] http://wise2.ipac.caltech.edu/docs/release/allsky/expsup/sec2_3f.html

where, for a given WISE band, λ is the isophotal wavelength, m_{zp} is the zero-point magnitude, and F^0_λ the corresponding flux of the magnitude zero-point in units of W cm^{-2} (Wright et al. 2010). It should be noted that this process integrates over any point sources overlapping with SNR extent. However, the subsequent analysis only employs the 22 μm WISE band magnitude, which is found to be free of stellar contributions and can be definitively associated with the source SNR (see §3.1).

2.4. *Radio Observations*

In this study, we also employ the results of F1998 and W1999, two additional survey papers examining radio continuum sources in the Magellanic Clouds and X-ray observations of LMC SNRs as performed by *ROSAT* respectively. F1998 uses the Parkes radio telescope at six frequencies (1.40, 2.30, 2.45, 4.75, 4.85 and 8.55 GHz) to catalog a total of 483 discrete radio sources in the LMC. They reference this catalog with a list of X-ray sources detected with *ROSAT* during Phase I of its operation (the *ROSAT* All-Sky Survey, or RASS) and, based on positional coincidence, identify the SNRs among their radio sources (F1998 – Table 2).

Of particular interest to the present work is the reported 4.75 GHz flux from each identified SNR (F1998 – Table 2, Column 4) and the relation given in F1998's §4.4.2 for converting this radio flux to a dynamic age of an individual SNR. This relation is based on the model of Chevalier (1982) for a Type II SN blast wave interacting with spherically symmetric, wind-blown stellar ejecta.[4] According to the model, Rayleigh-Taylor instabilities at the SN shock front may accelerate electrons via the amplification of magnetic fields. Van Buren & Greenhouse (1994) utilize this model to derive a relation between the observed 6 cm flux and the age of the SNR. By making use of distance estimates to the LMC and empirically calibrating the relation to the galactic remnant Cas A, F1998 arrives at the following formula:

$$S_{4.75} = 3887\, T^{-1.3} \tag{3}$$

where $S_{4.75}$ is the measured 4.75 GHz flux in Jansky (Jy) and T is the estimated age of the SNR in years. This relation is employed to estimate the ages of all SNRs within our source catalog having 4.75 GHz flux measurements.

2.5. *X-ray Observations*

Like F1998, W1999 also uses archival *ROSAT* data to examine LMC SNRs. However, W1999 makes use of pointed observations with the High Resolution Imager (HRI) from Phase II of *ROSAT*'s operation, which has higher angular resolution but lower X-ray sensitivity in the 0.1–2.0 keV energy range than the Position Sensitive Proportional Counter (PSPC) employed during the RASS. They report X-ray count rates for the 31 LMC SNRs detected by *ROSAT* (W1999 – Table 2, Column 3). For our present work, we convert these count rates to an X-ray luminosity multiplying the count rates by the energy conversion factor (ECF) provided in the text of W1999.

$$L_{X-ray} = C_{rate}\,(2 \times 10^{37} \mathrm{ergs\ s^{-1}}) \tag{4}$$

where L_{X-ray} is the total X-ray luminosity of the object, C_{rate} is the measured *ROSAT* HRI count rate, and the factor 2×10^{37} ergs s^{-1} is the ECF. The calculation of the ECF assumes that the SNRs are a collisionally-ionized plasma of temperature $\sim$ 0.5 keV, and an absorption column density to the LMC of $\sim 10^{21}$ cm^{-2}.

Additionally, the increased angular resolution of the HRI enables the analysis of the X-ray morphology of the LMC SNRs. W1999 proposes a classification scheme based on primary X-ray features of the SNR (W1999 – Table 4, Column 3). We summarize their classification scheme below (Table 1), and list the W1999 classifications of our sources in Table 2, Column 7.

TABLE 1
Williams et al. 1999 – X-ray Morphology

Designation	Description
Shell	near-complete limb that is brighter than face
Diffuse face	uniform brightness; limb may be indistinct
Centrally brightened	notably brighter than center of face
Peaked emission	dominated by central small bright source
Irregular	incomplete or nonexistent shell, patchy emission

3. ANALYSIS AND DISCUSSION

3.1. *22 μm Classifications*

WISE images of four example SNR from our source catalog, 0506-65.8, 0525-66.0, 0534-70.5, 0540-69.7, can be seen in Figure 1. Only a handful of SNR sources were observed in emission by WISE, with the most prominent SNR emission observed in the 22 μm band. The vast majority of SNRs are too faint in the 3.4 and 4.6 μm WISE images to be distinguished from background.[5] Additionally, the images are dominated by stellar (point-like) contributions, making the proposed integration scheme for calculating WISE band magnitudes (§2.3) for these bands unreliable.

The 12 μm emission observed in the WISE SNR-centered cut-outs is, in many cases, spatially extended beyond the SNR source region and has point-like sources present within this emission. Furthermore, all of our source SNR are observed in complex optical and/or Hα bright environments. We associate this type of optical emission with star-forming regions or areas of intense stellar activity. Hence, we interpret the observed 12 μm emission as stars embedded within a dusty surrounding medium. This extended 12 μm emission is more likely due to radiative excitation of PAH molecules from stellar sources than shock heating of grains or collisional excitation due to the expanding blast wave. When compared with the 22 μm emission morphologies observed for our sources, this conclusion is further justified. The 22 μm emission morphology of several sources can unambiguously be associated with SNR processes; as we observe

[4] While Chevalier (1982) is specifically modeling only Type II SNe, the interaction between a Type I SN blast wave and accreting stellar material would be expected to be similar in nature, save for geometric considerations.

[5] The exceptions to this rule are SNR 0525-66.1 (N49) and 0538-69.1 (N157B). These remnants, along with possible reasons for their emission in 3.4 and 4.6 μm, will be discussed in §3.4.

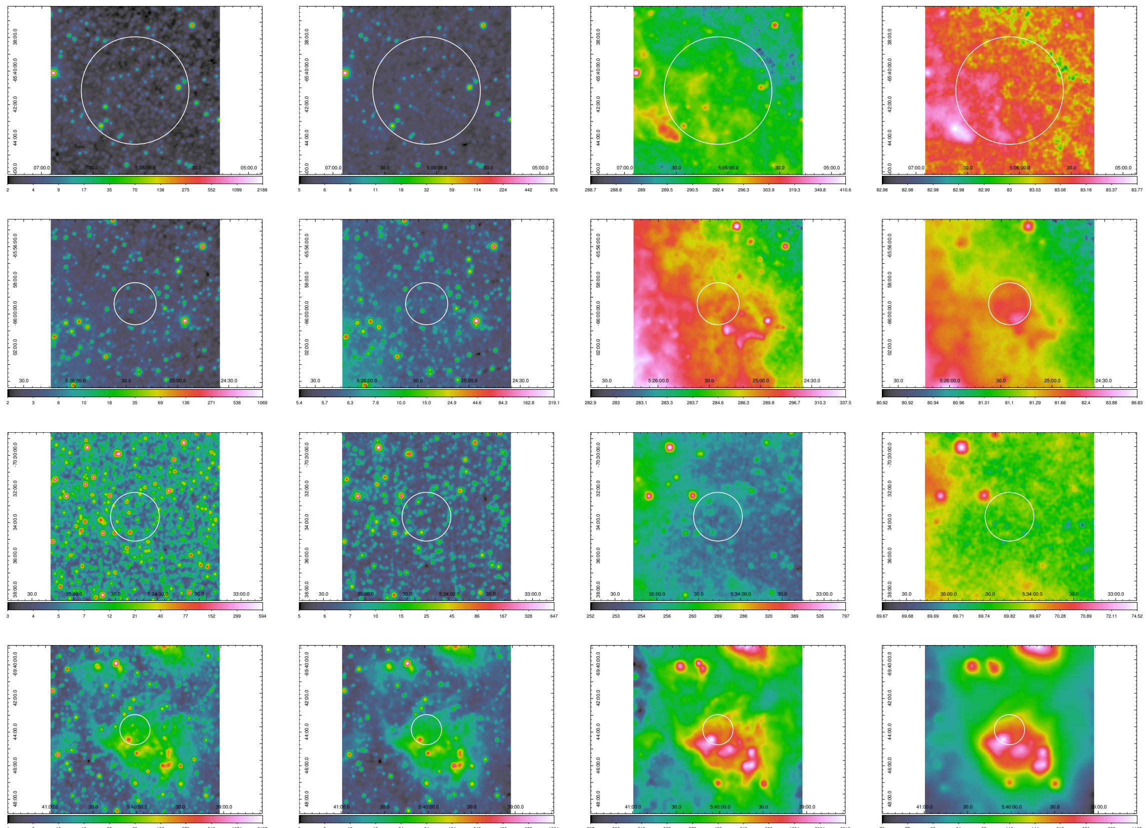

FIG. 1.— WISE observations of four LMC SNRs: 0506-65.8 (DEM L72, top row), 0525-66.0 (N49B, center top row), 0534-70.5 (DEM L238, center bottom row), and 0540-69.7 (SNR in N159, bottom row). These SNRs are shown in all four WISE bands, 3.4 μm (W1, leftmost column), 4.6 μm (W2, center left column), 12 μm (W3, center right column), and 22 μm (W4, rightmost column), and are chosen to be a representative sample of the compiled SNR source catalog.

no similar emission structure in 12 μm for the vast majority of our sources, we conclude the 12 μm is likely not associated with the SNR.

Rather distinct differences exist between LMC SNRs when observed in the WISE 22 μm band. As such, a classification system based on the 22 μm morphology of the SNR was employed to aid characterizing SNR/ISM interactions. We have used the following categories, Detected (D), Possible Detection (P), and Not Detected (N), to classify the SNRs within our catalog. The following primary characteristics were used in constructing these classes:

Detected (D): Emission is bright compared to background, roughly spherical, and fills (or nearly fills) the source region.

Possible Detection (P): Structured emission is present within the source region and is brightest on the periphery. Emission is point-like, clumpy, or asymmetric, and may or may not be associated with the presence of the SNR.

Not Detected (N): Emission within the source region either (1) is indistinguishable from background brightness and structure, (2) extends out of the source region and encloses a point-like feature, or (3) is comprised solely of point-like features.

These will henceforth be referred to as D-class, P-class, and N-class remnants respectively. Table 2, Column 6 lists how each source in our SNR catalog has been classified, and examples of each class of remnant can be found in Figure 2. A total of 10 SNRs were found to be D-class SNRs, 28 as N-class, 6 as P-class, and 1 (SN 1987A) was unresolved by WISE.[6]

3.2. *Temporal Evolution of X-ray, IR Emission*

Seeing as the population of LMC SNRs can be classified into three 22 μm morphological categories, we now seek the underlying physical causes of these categories. In particular, the D-class of remnants appears distinctly different than the two others, P-class and N-class, which have a more fluid classification criteria and hence may be more closely related.

Figure 3 is a plot of X-ray luminosity, calculated from the count rates of W1999 (§2.5), as a function of age estimated from the source's $S_{4.75}$ radio flux (§2.4). We have imposed our 22 μm morphological classification scheme to label the data points. Only 18 sources in our catalog have both *ROSAT* HRI and Parkes 4.75 GHz observations. Hence, we must bear in mind that the subsequent analysis may not accurately reflect the entire LMC SNR population since less than 50% of the possible sources

[6] A WISE-detected point source is found within $< 1''$ of the location of SN 1987A; however, with an angular resolution of $12''.0$ in the 22 μm band, WISE is unable to distinguish any of the remnant's interior detail.

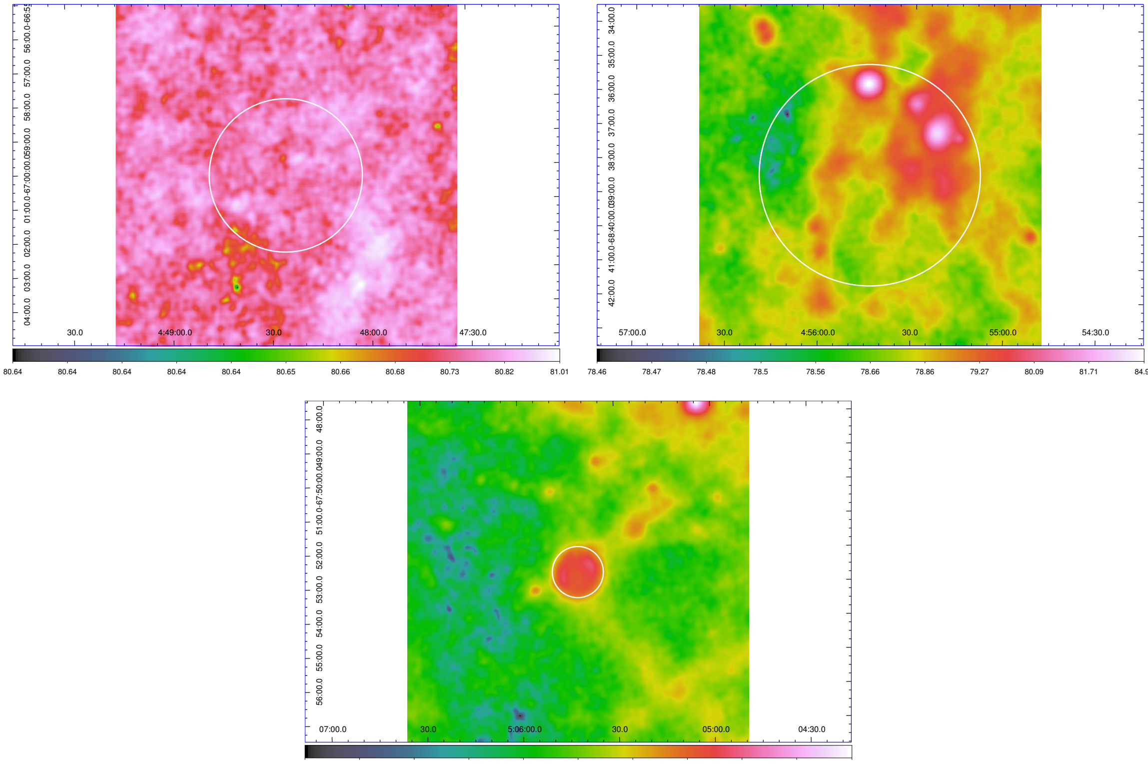

Fig. 2.— WISE 22 μm observations of three LMC SNRs within our source catalog. These remnants are archtypal members of each of the three 22 μm morphology classes. *Top Left*: MCELS J0448-6659, classified as Not Detected (N), *Top Right*: N86, classified as Possible Detection (P), *Bottom*: DEM L71, classified as Detected (D).

have the requisite W1999 and F1998 observations.

Most generally, Figure 3 shows that the X-ray luminosity of remnants diminishes with age; the X-ray luminosity of LMC SNRs peaks around 3×10^{37} ergs s^{-1} for most young ($\lesssim 2 \times 10^3$ years) remnants, and falls off to $\sim 2 \times 10^{35}$ ergs s^{-1} at ages $\gtrsim$ 5000 years). This is not surprising, as the SNR material cools over the X-ray lifetime of the SNR ($\sim 10^4$ years) and ceases to be hot enough to radiate in the X-ray. This decline in X-ray luminosity with remnant age also shows considerable scatter — the luminosities of remnants with approximately the same radio age can vary by as much as a factor of $\sim$100. This also is not surprising, since (1) the radio age may underestimate the age of the remnant, as Eq. 3 assumes that all 4.75 GHz radio emission is due to magnetically-accelerated electrons at the shock front and (2) variety in the ambient ISM composition and density can dramatically change the efficiency of X-ray line emission for ejecta-dominated remnants.

Examining Figure 3 in terms of 22 μm morphological categories, one finds that the D-class remnants are generally both the youngest remnants ($\lesssim$ 2000 years, with one exception at $\sim$ 4000 years) and the most X-ray bright ($\gtrsim 10^{36}$ ergs s^{-1}). These are contrasted with the population of N-class remnants, which are less X-ray luminous and typically older. The distinction between these two classes in Figure 3 suggests that the luminous, spherical 22 μm emission from these D-class SNR is likely not solely an environmental effect, e.g. due to the presence or absence of large grain dust in the ISM. Were the effect solely environmental, we would expect to find D-/N-class remnants at a variety of different ages/X-ray luminosities. Instead, the distinct grouping of D-/N- class remnants by age and X-ray luminosity implies that the 22 μm morphology observed is age-dependent, and hence tied to the dynamic evolution of the SNR.

To investigate this supposition, we plot the integrated 22 μm flux $f_{22\mu m}$ as a function of remnant age T (Figure 4). Only the 7 D-class remnants whose 4.75 GHz radio flux has been measured are considered here; we limit ourselves to D-class remnants as, by definition of the 22 μm categories, it is unclear if the 22 μm emission present in the source region of P-/N- class remnants is associated with the SNR/ISM interaction or due to a background source. This trend was also fit with a function of the form $f_{22\mu m}(T) = c\,(T/1000 \text{ years})^{-a}$, where the parameters c and a were found using the *optimize* routine in Python's Scipy package. The best fit parameters were found to be $a = 2.84 \pm 0.27$, $c = (4.02 \pm 1.67) \times 10^{-18}$ W cm^{-2}. Figure 4 clearly shows that the strength of the 22 μm emission for D-class remnants diminishes over time, further strengthening the case that the observed 22 μm morphology is an age-dependent effect. The power-law behavior of the 22 μm flux with age appears to effectively flatten after $T \sim 4000$ years, suggesting that the mechanism for producing this emission is no longer efficient on longer timescales.

3.3. *D-class SNRs — what are they?*

Based on these observations, we conclude that spherically structured 22 μm emission characterizing D-class remnants is likely due to ISM dust which was not swept-

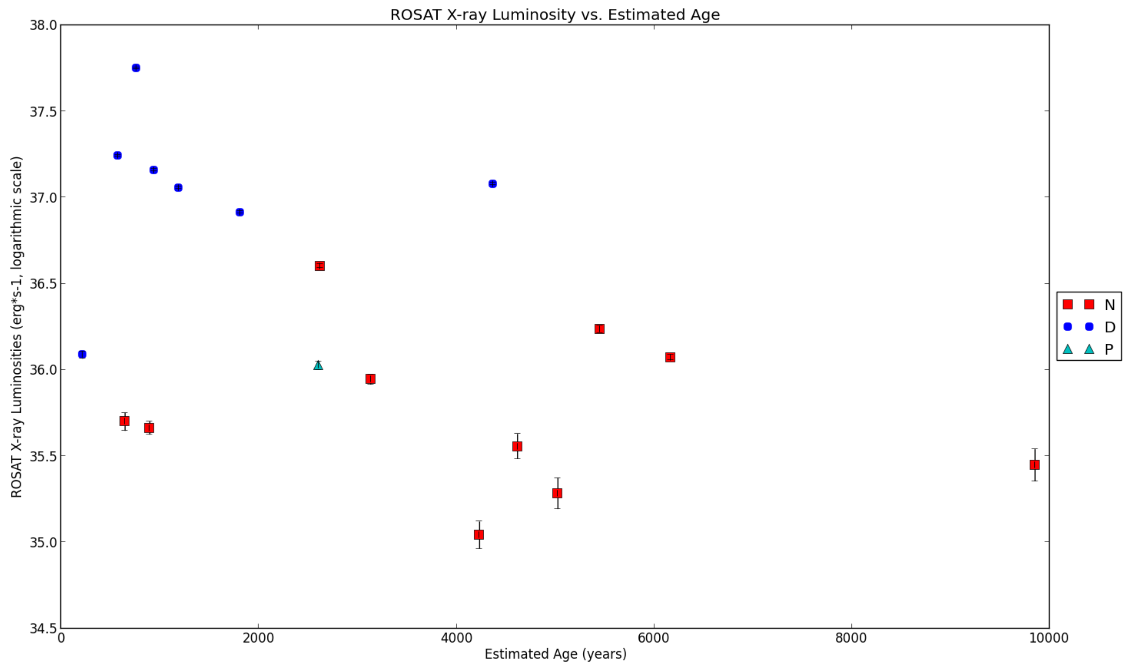

Fig. 3.— X-ray luminosities and estimated ratio ages for 18 source SNR having both *ROSAT* HRI observations and measurements of their 4.75 GHz flux. The points are labeled by our 22 μm classification scheme, D being Detected (blue circles), P being Possible Detections (green triangles), and N being Not Detected (red boxes).

up by the SN blast wave, but nevertheless was strongly shocked and heated. The relatively high X-ray luminosity of the D-class remnants and comparatively young age implies that the SN is either still in the "free-expansion" phase or in the early stages of SNR adiabatic expansion, both of which are characterized by strong shocks. These shocks heat large dust grains in the ambient ISM, causing the observed thermal emission at 22 μm (small grains and PAHs do not contribute to the 22 μm WISE band, see §2.2).

The roughly spherical structure of the 22 μm emission is also consistent with the idea of heating from SNR-associated shocks. Early in the SNR lifetime, the blast wave would be expected to propagate isotropically (modulo any explosion asymmetries) out from the progenitor star since, during the free-expansion phase of the SNR, any density inhomogenities in the ambient medium would be smoothed out by the SN blast wave. Given the relative youth of the D-class remnants, we would thus expect already shocked material to trace out a roughly spherical structure, congruent with the idea that the 22 μm emission is the result of shocked dust. Rather than deforming the blast wave, any density inhomogenities in the ISM encountered at such a young expansion time would appear as bright knots of emission due to the excess shocked material present there. This knot-like substructure is indeed observed with the D-class spherical emission shell. Finally, relying on shocked large grain dust as the mechanism for the observed 22 μm emission hints at the possibility that a young remmant may not appear to be a D-class remnant if the ambient medium is sufficiently devoid of large grains and/or comparatively underdense. This may be the case for the N-class remnants having radio ages of $\lesssim$ 2000 years that were not classified as D-class remnants. In sum, D-class remnants must not only be young, but the ambient environment must be sufficiently "dusty" i.e. have a significant large dust grain population to account for the 22 μm emission.

The spherical 22 μm morphology also indicates that the large dust grains are spread throughout the interior of SNR. As large dust grains typically trace regions of high ISM density, it is possible that the interior may yet be a region of high density for D-class remnants. This is in keeping with the W1999 X-ray morphology classifications of D-class remnants. Eight of the 10 D-class remnants in our study have either "Shell" or "Diffuse Face" W1999 X-ray morphology classifications. These classifications imply that the shocked material on the edge of the blast wave is responsible for the bulk of the observed X-ray emission, and hence has either been heated to a higher temperature than the interior material or that the outer blast wave material has sufficiently low densities to radiate in the X-ray. Given the evidence for shock heating in the remnant interior, the latter seems more likely.

3.4. *Dust Destruction*

Given the absence of SNR-associated 3.4, 4.6, and 12 μm emission for the majority of our sources and the decline in 22 μm flux over time for D-class remnants observed in Figure 4, it is plausible we are witnessing SNR dust destruction throughout the population of LMC remnants. Borkowski et al. 2006 examines the possibility of dust destruction for four Type Ia SN in the LMC using *Spitzer* Infrared Array Camera (IRAC) and Multiband Imaging Photometer for Spitzer (MIPS) observa-

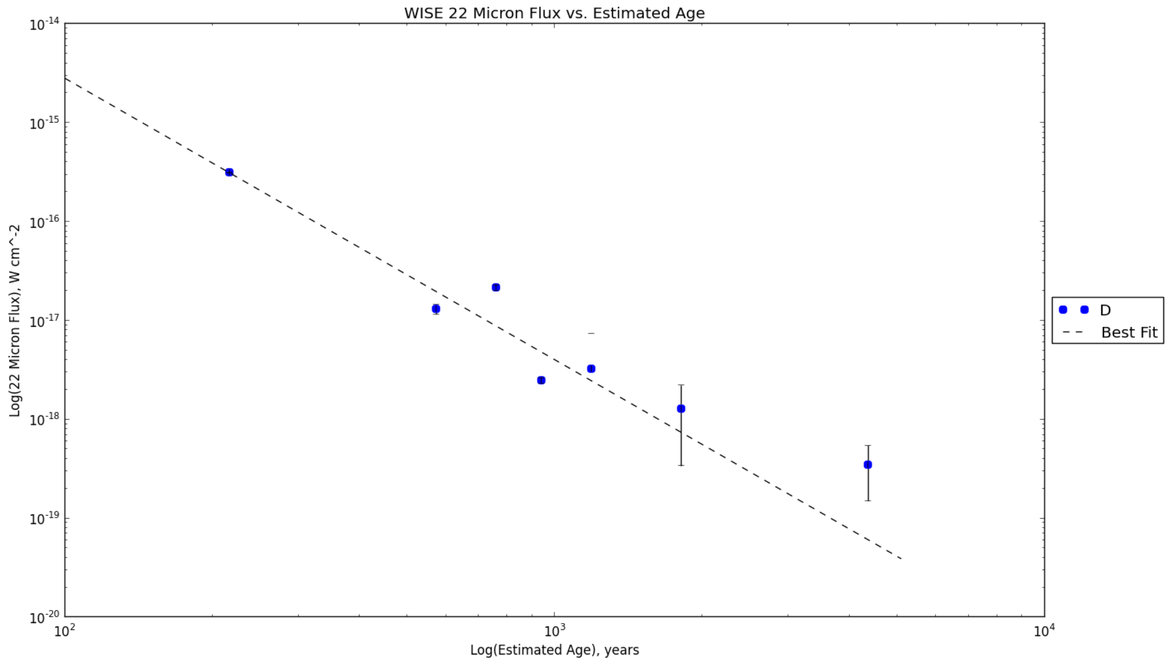

FIG. 4.— Measured 22 μm fluxes and estimated ratio ages for SNRs classified as Detected (D) remnants under the 22 μm morphology classification scheme. Only 7 such remnants have measured 4.75 GHz radio fluxes. The dashed line overplotted is a best-fit model of the decline of 22 μm flux ($f_{22\mu m}$) with remnant age T to the functional form $f_{22\mu m}(T) = c\,(T/1000 \text{ years})^{-a}$. The best-fit parameters are found to be $a = 2.84 \pm 0.27$, $c = (4.02 \pm 1.67) \times 10^{-18}$, where c has units of W cm^{-2}.

tions. Three of these four (SNR 0505-67.9, 0509-67.5, 0519-69.0) are classified as D-class remnants in our study, while the fourth SNR, 0548-70.4, is classified as N. They conclude that the SNRs are efficient destroyers of PAHs, given their nondetection of emission in the IRAC bands, and find that their MIPS observations can be reproduced by a collisionally heated dust model, provided the model allows for the destruction of small dust grains. We concur with Borkowski et al. 2006, and extend their conclusion beyond Type Ia remnants to the broader LMC SNR population: as we observe few instances of SNR-associated 3.4, 12 μm emission from sources within our catalog, we find that PAHs are efficiently destroyed by most SNRs. Furthermore, the lack of 4.6 μm emission from the majority of LMC SNRs is likely indicates the destruction of small grains, as was also found by Borkowski et al. 2006.

There are, however, exceptions to the lack of observed emission in the 3.4, 4.6 and 12 μm WISE bands. Two LMC remnants, SNR 0525-66.1 (N49) and 0538-69.1 (N157B), are observed to have emission at these wavelengths which traces the 22 μm emission previously associated with the SNR (Figure 5). Both SNR 0525-66.1 and 0538-69.1 are D-class remnants, have bright knots of emission offset from the center of the SNR source region, and are exceptionally young remnants (T ~600 years and ~200 years respectively). The presence of SNR-associated 3.4, 4.6 and 12 μm emission in these two remnants may indicate that the PAHs and small dust grains responsible for the emission in the first three WISE bands may not be completely destroyed within SNR on timescales $\lesssim$ 500 years. The (non-)destruction of PAHs and small grains may also be dependent on the ambient ISM density. Rather than having a uniform brightness over the SNR extent, SNR 0525-66.1 and 0538-69.1 possess bright knots of emission that are spatially coincident in all four WISE bands, consistent with the presence of a local excess of shocked material. Within this overdense region, the population PAHs and small dust grains may not be destroyed as rapidly due to the relative overabundance of material. Furthermore, SNR 0519-69.7 (SNR in N129) and 0547-69.7 (DEM L316B) have similar ages (T ~600 years and ~900 years respectively) but are not observed in 3.4, 4.6 and 12 μm emission. Given the small variation in radio ages between these two groups of young remnants, we interpret this as an environmental, as opposed to evolutionary, difference between SNR 0525-66.1, 0538-69.1 and 0519-69.7, 0547-69.7.

The decline in 22 μm emission with remnant age for D-class remnants (Figure 4) suggests that some shock-associated process is also affecting large dust grains. It is possible that this trend represents dust cooling as the SNR evolves, by which the large grain population has radiated away enough of the shock-deposited energy to no longer radiate in 22 μm. Yet this seems unlikely: as the grains are in a turbulent environment, likely interacting with multiple shock fronts over this timescale (~4000 years), we would expect this population to be reheated after the initial shock.

Therefore, we posit that this trend is due to the destruction of large grains over the remnant's lifetime. Destruction of large grains is possible through shock-driven, collisional processes, by which the dust volume is continuously eroded, or by sublimation through continued exposure to electrons/ions at X-ray plasma temperatures

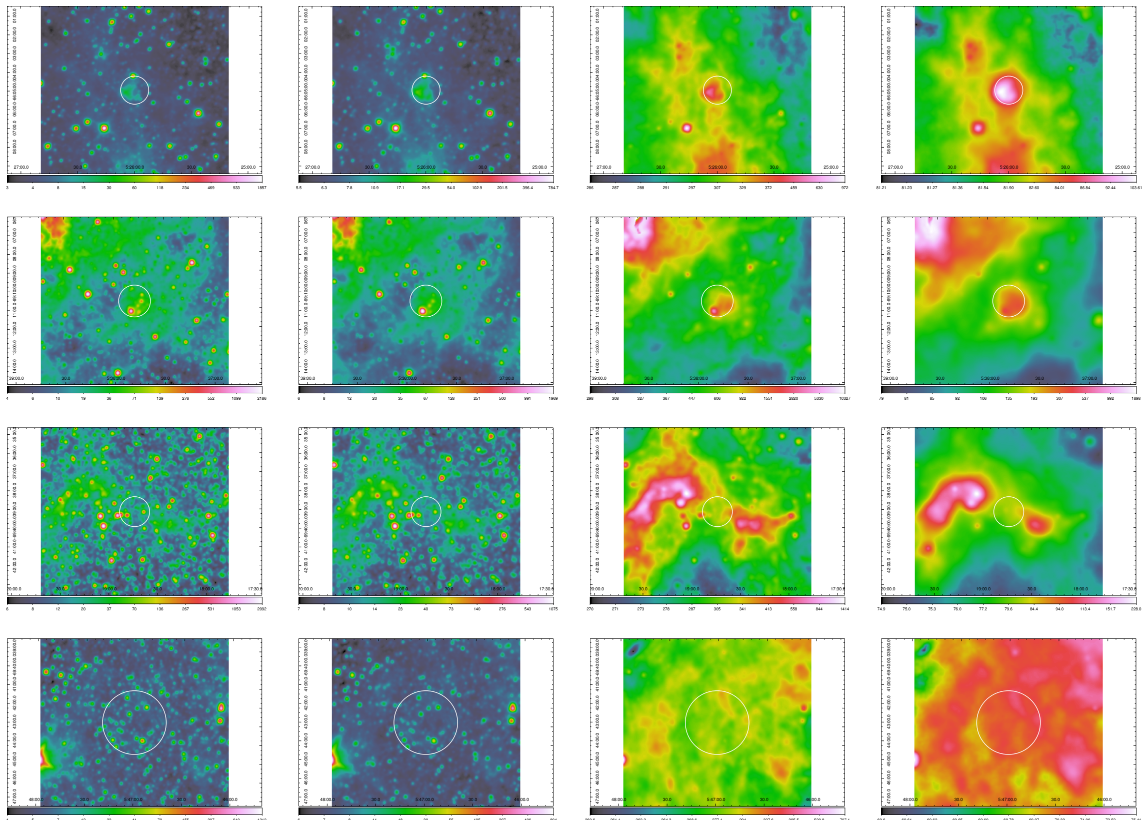

FIG. 5.— WISE observations of four LMC SNRs: 0525-66.1 (N49, top row), 0538-69.1 (N157B, center top row), 0519-69.7 (SNR in N120, center bottom row), and 0547-69.7 (DEM L316B, bottom row). The four columns correspond to the four distinct WISE bands: 3.4 μm (W1, leftmost column), 4.6 μm (W2, center left column), 12 μm (W3, center right column), and 22 μm (W4, rightmost column). The topmost remnants, 0525-66.1 and 0538-69.1, are both D-class remnants and are notable in that they are detected in emission in the lower three WISE bands (3.4, 4.6, and 12 μm), unlike the majority of LMC SNRs. The SNRs displayed on the two bottom rows, 0519-69.7 and 0547-69.7, have similar ages but are N-class remnants; these are shown for comparison.

($\geq 10^6$ K). This process also better explains the fitted power-law decline of the 22 μm emission. As the underlying population of dust grain is anticipated to have a power-law distribution in size (Draine & Li 2007), the decay of the observed emission could be due to the destruction of the large grain population "from the bottom-up", i.e. the smallest grains surviving the initial shock are destroyed first, followed by the largest grains on longer timescales. Detailed simulations are needed to determine whether this hypothesis of large dust grain destruction is likely under SNR conditions, and which process (sublimation or collisional erosion) is predominant.

3.5. *YSOs Associated with SNRs*

WISE probes two distinct IR regimes of the ISM relevant to SNR interactions with its four bands: 3.4 and 12 μm contain prominent PAH features, molecular conglomerate structures that are weakly bound as the particles cool; 4.6 and 22 μm trace, on the other hand, the thermal emission from both large and small grains (Wright et al. 2010). Thus, WISE can uniquely be used to characterize both the heating and cooling of interstellar environments, a precondition for star formation in the ambient medium.

Specifically, the SNRs considered here are mostly observed in 22 μm due to the energetic destruction of any local PAHs, while young stellar objects (YSOs) can be found primarily in the first three WISE bands as they represent the early evolution of gravitationally locked material into stars. Whereas SNRs are diffuse sources due to their large spatial scales, YSOs can be identified by point-like emission. We therefore utilize a photometric procedure proposed by Koenig et al. 2012 to search through the WISE point source catalog for any YSO candidates located within $10'$ (≈ 150 pc at LMC distance) of our SNR sample that may be associated with a remnant induced star formation event.

Out of all possible nearby point sources surrounding each SNR in the WISE image planes, one must assume that the YSOs are localized in a multidimensional color space due to their specific IR emission signature. In order to reduce the contamination of extraneous objects, we apply several "color-cuts," or color magnitude cutoffs, in the plane of a color-color diagram for multiple combinations of the WISE bands. The following objects are removed in sequence: star forming galaxies that exhibit PAH-feature emission contributing to a redder color, broad-line AGNs faint in the mid-IR compared to YSOs, shock emission knots primarily seen in 4.6 μm, and structured PAH emission confused as a point source in 12 μm.

From the remaining list of objects, the YSOs are identified by good detections with an uncertainty <0.2 mag in the 3.4, 4.6, and 12 μm bands. These surviving candidates constitute both protostars and T Tauri stars with the possibility of including a margin of 5 false YSOs per square degree for an outer Galactic region like the LMC

(Koenig et al. 2012). We estimate that in each 10′ radius cone around the SNRs considered at most one false detection will occur. The final selected YSO candidates are distributed among 17 SNRs with about half of the sample likely being contaminated; the neighboring SNR and the coordinate positions of each YSO are listed in Table 3.

3.6. *SNR Shock-triggered Star Formation*

It is observationally motivated that strong shocks can trigger star formation in molecular cloud regions through perturbation of the self-gravitating system (Thompson et al. 1998, Chen et al. 1993). However, evidence for the presence of an SNR causing this type of activity is less clear (Herbst & Assousa 1997). D2010 investigates such a possibility in the LMC using optical MCELS observations of SNRs and molecular clouds (MCs) in conjunction with a catalog of known YSOs to search for spatial association, but concludes that no causality can be determined for the 10 likely SNR/YSO pairings found because of the disagreement between the age of the YSOs and dynamical time-scales of the SNRs.

We expand upon this study by employing an IR follow-up using WISE observations to capture SNR morphology in the local environment and detect nearby YSO candidates through a color-magnitude cut-off scheme (Koenig et al. 2012). No cross-confirmation was attempted between the WISE-identified YSOs and a derived YSO catalog; nonetheless, this does not preclude the possibility of including newly discovered objects. From the 17 obtained SNRs paired to several YSOs within a 10′ conical region, the 10 SNR considered by D2010 are accounted for in this sample. To establish the plausibility of a triggering event, we subject the sources in Table 3 to three criteria: (1) located in spatial proximity to the SNR 22 μm emission profile, ignoring any possible projection effects, (2) matched to significantly old SNR implying a gentle shock front, and (3) associated with a structured molecular environment.

Six SNR are found to have closely associated YSOs lying along or within the emission detection in WISE band 22 μm. They are: SNR 0525-66.1, 0532-67.5, 0535-69.3, 0536-67.6, 0538-69.1, 0540-69.3. In the cases of SNR 0532-67.5, 0536-67.6, and 0538-69.1, D2010 dismisses an unambiguous relationship to the YSOs due to projection effects, YSOs may lie outside the boundary of the SNR, and the complexity of the molecular region, YSOs may be associated with other neighboring objects. D2010 also offers a possible explanation for the close alignment examined here; the matched SNR may have originated within an interstellar bubble blown out by the progenitor star. The mild expansion velocity of the bubble could then induce star formation, while the low density of the interior would allow for a rapid catchup of the growing SNR boundary to converge on any already forming YSOs.

Of these SNR, only four (0525-66.1, 0532-67.5, 0536-67.6, and 0538-69.1) were sufficiently observed in radio emission by F1998 to determine ages as a proxy for shock speed. However, none of these sources are older than 10^3 years, implying that the shocks are still moving fast enough to destroy nearby molecular cloud cores rather than incite star formation. A more accurate comparison, used by D2010, would be the actual spectral measurement of expansion velocity. Even the temporal association of the SNR to the YSOs situated at the boundary of emission is not explicit evidence for the interaction of the SNR with the YSO progenitor. As the timescale of collapse for a YSO is $\sim$ 1 Myr, it is plausible that the YSO began collapsing well before the SN event, and thus does not represent triggered star formation.

Another means of evaluating the importance of SNR shock-triggered star formation in the LMC is via the comparison of the star-formation and SNR birth rates. F1998 estimated an SNR birth rate of one every 100 ($\pm$20) yr compared to a calculated star-formation rate of 0.7 ($\pm$0.2) $M_\odot$ yr^{-1} in the LMC. Thus, in order for SNR perturbation to be a significant mechanism for star formation in the LMC, each SN event must trigger the formation of $\sim$ 50–100 stars. This number is plausible in active SFRs, but may be too high for isolated SN events. A relatively complete survey counting the number of LMC YSOs, as well as a measurement of their respective ages, would be required to determine whether this number of triggered events is reasonable.

Lastly, we examine if any of the spatially identified SNR/YSO pairings occur in regions of molecular structure. The environment of an SNR can provide evidence as to the nature of the SN progenitor star as well as the primordial material forming other stars. Chu et al. 1988 (hereafter C1988) analyzed the known SNR in the LMC to divide them into two distinct classes that we adopt here: "Pop I" SNR arise from the collapse of massive (> 10 $M_\odot$) stars and "Pop II" SNR form from the thermonuclear reaction of a white dwarf. While this classification scheme does not necessarily coincide with Type Ia and II SNe, the criteria for each are significant to this study. Specifically, C1988 identifies Pop I SNRs with OB associations and HII regions, implying that these SNR have a quick turnover into a rich environment. The Pop II designation, on the other hand, is difficult to unambiguously assign and is left for young isolated systems.

From our refined sample, C1998 labels SNR 0525-66.1, 0536-67.6, 0538-69.1, and 0540-69.3 as Pop I, clarifying why YSOs could be found in vicinity of SNR. Another study of star forming regions carried out by Koenig et al. 2012 with WISE, observed "pillar" and "trunk-like" structures of diffuse emission in 12 and 22 μm surrounding selected YSO objects. We confirm that the SNR/YSO pairs (Table 3) are seen near densely structured emission in the IR and further identify these clouds as entwined with primarily Hα gas as found in MCELS optical filters. The young ages for the SNRs considered and the complex environments they are contained in, however, lead to the rejection of all possible direct productions of spatially associated YSOs.

4. SUMMARY

By using observations from the WISE All-Sky Survey and making use of the compiled WISE Point-Source Catalog, we are able to investigate the interaction between SNRs and the surrounding ISM within the LMC. We find that the LMC contains three distinct populations of SNRs, which can be categorized based on their observed morphology in the WISE 22 μm band (W4). The lack of emission in the 3.4, 4.6, and 12 μm WISE bands implies that the SNRs are destroying components of the ISM through shock dissociation and heating. The observed 22 μm emission appears to be driven by the shock heating of large grain ISM dust, and depends on both the age of the remnant and possibly the relative abundance of large dust grains. The power-law decline of 22 μm flux $f_{22\mu m}$ with remnant age T (as calculated from radio flux $S_{4.75}$) suggests that the population of large grains in the interior of the remnant is changing over the SNR's evolutionary lifetime, either cooling sufficiently after ∼4000 years that it no longer radiates in 22 μm or being destroyed through sublimation due to shock heating. Theoretical calculations are needed to determine which mechanism, cooling or destruction, is responsible for the diminishing 22 μm brightness with remnant age, and should be examined in a future paper.

In addition, the possibility of shock-triggered star formation from SNRs was investigated by use of the WISE Point-Source Catalog. This study locates 36 YSO candidates within a $10'$ cone around SNRs in the LMC, and 6 LMC SNRs are found to have close spatial association with these YSO candidates. However, no source SNR spatially associated with a YSO candidate is found to be old enough ($\sim 10^4$ years) so as to have a slow shock velocity. These shocks would not perturb, but instead destroy, a molecular cloud core (Boss 1995, Foster & Boss 1996). Thus, we observe no evidence for SNR shock-triggered star formation within the LMC. Furthermore, based on this observation as well as the estimated SNR birth rate and the star-formation rate of the LMC, we conclude that SNR shock-triggered star formation is not likely an important mechanism for star formation.

It must be acknowledged, however, that searches for SNR shock-triggered star formation using our criteria possess a significant selection bias. No LMC SNR within our source catalog is old enough to meet the condition of slow shock velocities (see §3.6, criterion #2), and such aged remnants would appear too dim to identify in optical or X-ray observations. Thus, while we find no evidence for SNR shock-triggered star formation in the LMC from direct SN blast wave/molecular cloud core interactions, shocks from old SNR may still contribute to general ISM turbulence and help trigger star formation.

Both the 22 μm morphology and the SNR shock-triggered star formation investigations were made possible by comparing observations across multiple wavelengths (radio, IR, optical and X-ray). Such a synthesis of observational information can provide valuable insight as to the interaction between the ISM and SNRs in a variety of density/temperature regimes, and will be necessary to untangle the complex processes governing the evolution of the ISM.

C. DeRoo wishes to acknowledge his wife, who was very supportive during his frustrating attempts to learn Python. S. De Pascuale wishes to acknowledge the coffee machine in his office, which provided the necessary motivation to perform this work.

Facilities: WISE.

REFERENCES

Andersen, M., Rho, J., Reach, W. T., Hewitt, J. W., & Bernard, J. P. 2011, ApJ, 742, 7
Badenes, C., Maoz, D., Draine, B. T. 2010, MNRAS, 407, 1301
Borkowski, K. J. et al. ApJ, 2006, 642, L141
Boss, A.P. 1995, ApJ, 439, 224
Chen, H., Tokunaga, A. T., Strom, K. M., & Hodapp, K.-W. 1993, ApJ, 407, 639
Chevalier, R. A. 1977, Ann. Rev. Astron. & Astrophys., 15, 175
Chu, Y.-H., Kennicutt, R. C. 1988, AJ, 96, 6
Desai, K. M. Chu, Y.-H., Gruendl, R. A., Dluger, W., Katz, M., Wong, T., Rosie Chen C. H., Looney, L. W., Hughes, A., Muller, E., Ott, J., & Pineda J. L. 2010, AJ, 140, 584
di Benedetto, G. P. 2008 MNRAS, 390, 1762
Draine, B. T. & Li, A. 2007, ApJ, 657, 810
Fesen, R.A., Blair, W. P., & Kirshner, R. P. 1985, ApJ, 292, 29
Foster, P. N. & Boss, A. P. 1996, ApJ, 468, 784
Foster, P. N. & Boss, A. P. 1997, ApJ, 489, 346
Fukugita, M., & Peebles, P. J. E. 2004, 616, 643
Green, D. A. 2009, Bull. Astr. Soc. India, 37, 45
Herbst, W. & Assousa, G. E. 1977, ApJ, 217, 473
Klein, R. I., McKee, C. F., & Colella, P. 1994, ApJ, 420, 213
Maggi, P., Haberl, F., Bozzetto, L. M., Filipoviċ M. D., Points, S. D., Chu, Y.-H., Sasaki, M., Pietsch, W., Gruendl, R. A., Dickel, J., Smith, R. C., Sturm, R., Crawford, E. J. & De Horta, A. Y. 2012, A&A, 546, A109
Mathewson, D. S., Ford, V. L., Dopita, M. A., Tuohy, I. R., Long, K. S., & Helfand, D. J. 1983, ApJS, 51, 345
Mathewson, D. S., Ford, V. L., Dopita, M. A., Tuohy, I. R., Mills, B. Y., & Turtle, A. J. 1984, ApJS, 55, 189
Mathewson, D. S., Ford, V. L., Tuohy, I. R., Mills, B. Y., Turtle, A. J., & Helfand, D. J. 1985, ApJS, 58, 197
Micelotta, E. R., Jones, A. P., & Tielens, A. G. G. M. 2010, A&A, 510, A36
———, 2010, A&A, 510, A37
Reach, W. T., Rho, J., Tappe, A., Pannuti, T. G., Brogan, C. L., Churchwell, E. B., Meade, M. R., Babler, B., Indebetouw, & Whitney, B. A. 2006, AJ, 131, L1479
Russell, S. C., & Dopita, M. A., 1992, 384, 508
Draine & Salpeter. 1979, ApJ, 231, 438
Sedov, L. I. 1959, Similarity and Dimensional Methods in Mechanics (New York: Academic)
Stone, J. M., & Norman, M. L. 1992, ApJ, 390, L17
Thompson, R. I., Corbin, M. R., Young, E., & Schneider, G. 1998, ApJ, 492, L177
Tappe, A., Rho, J., & Reach, W. T., 2006, ApJ, 653, 267
Williams, R. M., Chu, Y.-H., Dickel, J. R., Petre, R. Smith, R. C., & Tavarez, M. 1999, ApJS, 123, 467
Wright et al. 2010, AJ, 140, 1868
Vanhala, H. A. T., & Cameron, A. G. W. 1998, ApJ, 508, 291
Van Buren D., Greenhouse M.A., 1994, ApJ 431, 640
van der Marel, R. P. & Cioni, M.-R. L. 2001, ApJ, 122, 1807

Table 2
Supernova Remnants in the Large Magellanic Cloud - Coordinates and Characteristics

Object Number (B1950)	Object Name	RA (J2000) (hh mm ss)	Dec (J2000) (ddd mm ss)	Angular Size (arcmin)	22 μm Morph. Class	22 μm Flux (10^{-18} W cm^{-2})	X-ray Morph. (W1999)
0448-67.1	MCELS J0448-6659	04 48 25	-67 00 12	4.5	N	-	N
0449-69.4	MCELS J0449-6921	04 49 22	-69 20 25	2.0	N	-	N
0450-70.9	SNR 0450-709	04 50 30	-70 50 05	7.7	N	-	X
0453-66.9	SNR in N4	04 53 14	-66 55 42	4.3	P	-	I
0453-68.5	SNR 0453-685	04 53 38	-68 29 27	2.0	N	-	DF
0454-67.2	SNR in N9	04 54 33	-67 13 00	2.8	N	-	CB
0454-66.5	N11L	04 54 50	-66 25 37	1.4	N	-	I
0455-68.7	N86	04 55 44	-68 38 23	6.5	P	-	I
0500-70.2	N186D	04 59 56	-70 07 58	2.6	N	-	N
0505-67.9	DEM L71	05 05 42	-67 52 39	1.5	D	1.07	S
0506-68.0	N23	05 05 55	-68 01 47	1.2	D	1.27	I
0506-65.8	DEM L72	05 06 06	-65 41 08	6.4	N	-	N
0509-68.7	N103B	05 08 59	-68 43 35	0.50	D	2.46	S
0509-67.5	SNR 0509-675	05 09 31	-67 31 17	0.56	D	9.20×10^{-2}	S
0513-69.2	SNR 0513-692	05 13 14	-69 12 08	4.5	N	-	X
0519-69.7	SNR in N120	05 18 44	-69 39 09	1.6	N	-	CB
0519-69.0	SNR 0519-690	05 19 35	-69 02 09	0.55	D	3.47×10^{-1}	S
0520-69.4	SNR 0520-694	05 19 46	-69 26 00	2.4	N	-	DF
0522-65.8	MCELS J0521-6542	05 21 39	-65 43 10	3.0	N	-	N
0523-67.9	SNR in N44	05 23 06	-67 53 06	3.5	N	-	DF
0524-66.4	DEM L175a	05 24 18	-66 24 19	4.1	N	-	X
0525-69.6	N132D	05 25 04	-69 38 28	2.0	D	2.50×10^{1}	S
0525-66.0	N49B	05 25 25	-65 59 22	2.5	D	3.25	DF
0525-66.1	N49	05 26 00	-66 04 57	1.5	D	1.30×10^{1}	DF
0528-69.2	SNR 0528-692	05 27 39	-69 12 04	2.7	N	-	U
0527-65.8	DEM L204	05 27 57	-65 50 00	4.5	N	-	X
0531-70.2	MCELS J0530-7008	05 30 44	-70 07 10	3.5	P	-	N
0532-71.0	SNR in N206	05 31 56	-71 00 19	3.0	N	-	CB
0532-67.5	SNR 0532-675 in N57	05 32 30	-67 31 33	4.5	N	-	N
0534-69.9	SNR 0534-699	05 34 02	-69 55 05	1.7	N	-	DF
0534-70.5	DEM L238	05 34 18	-70 33 26	2.9	N	-	U
0535-69.3	SNR 1987A	05 35 28	-69 16 11	0.1	U*	-	U
0535-66.0	N63A	05 35 44	-66 02 14	1.4	D	2.14×10^{1}	DF
0536-69.3	Honeycomb	05 35 48	-69 18 04	1.4	N	-	I
0536-67.6	DEM L241	05 36 03	-67 35 04	2.4	P	-	X
0536-70.6	DEM L249	05 36 07	-70 38 37	3.0	N	-	U
0538-66.5	DEM L256	05 37 30	-66 27 47	3.6	P	-	N
0538-69.1	N157B	05 37 48	-69 10 35	1.7	D	3.12×10^{2}	PE
0540-69.7	SNR in N159	05 40 00	-69 44 02	1.8	P	-	U
0540-69.3	N158A	05 40 12	-69 19 55	1.3	N	-	PE
0543-68.9	DEM L299	05 43 10	-68 58 49	5.8	N	-	U
0547-69.7	DEM L316B	05 47 00	-69 42 55	3.4	N	-	S
0547-69.7	DEM L316A	05 47 22	-69 41 26	2.0	N	-	DF
0548-70.4	SNR 0548-704	05 47 49	-70 24 53	2.0	N	-	DF
0551-68.4	SNR J0550-6823	05 50 30	-68 23 22	5.2	N	-	N

Table 2: Catalog of sources used in this study, adapted from D2010. Angular size (Column 5) is the radius of the circular extraction region used to compute 22 μm brightnesses (see §2.3). 22 μm morphological classes (Column 6) are assigned from the following categories: Not Detected (N-class), Possible Detection (P-class), and Detected (D-class). N-class remnants have no SNR-associated 22 μm emission above background levels, P-class remnants have structured 22 μm emission on the periphery of the SNR source region, but it is unclear whether said emission is associated with the SNR, and D-class remnants possess a distinct spherical emission structure filling nearly the entire source extent. For D-class remnants, the calculated 22 μm flux $f_{22\mu m}$ is reported in units of W cm^{-2} (Column 7). X-ray morphology classifications (Column 8) are taken from W1999, and can be summarized as follows: *Shell* (S) — near-complete limb that is brighter than face; *Diffuse Face* (DF) — uniform brightness; limb may be indistinct; *Centrally Brightened* (CB) — notably brighter than center of face; *Peaked emission* (PE) — dominated by central small bright source; *Irregular* — incomplete or nonexistent shell, patchy emission; *No Data* (N) — no *ROSAT* observation for classification; *Not Mentioned* (X) — not mentioned in W1999 source catalog, possibly undiscovered at time of W1999 publication.

Table 3
YSO Candidates

SNR (catalog)	YSO (J2000)	
Object Number	R.A. (deg.)	Dec. (deg.)
0449-69.4	72.3178282	-69.3466413
0454-67.2	73.6936261	-67.2212584
	73.6884129	-67.2234927
0455-68.7	73.9489095	-68.6218472
	73.8373958	-68.6446956
0513-69.2	78.357028	-69.1754465
	78.3711563	-69.191889
0523-67.9	80.740559	-67.8885923
0524-66.4	81.0397654	-66.4039656
	81.0365843	-66.3970775
0525-66.1	81.504825	-66.0772253
	81.4953056	-66.0883358
	81.5182736	-66.0843203
	81.4917777	-66.0837952
0532-71.0	82.9481305	-71.0105885
	82.9387694	-71.0238692
0532-67.5	83.1259954	-67.5262646
0535-69.3	83.8665813	-69.269717
0535-66.0	83.9508009	-66.0335117
0536-67.6	83.9741573	-67.5912925
	83.9718254	-67.5883997
	84.0112797	-67.5651773
	84.0453732	-67.5763887
	83.9915404	-67.5895216
	84.0120214	-67.5701677
0538-66.5	84.3089618	-66.4499308
	84.4258839	-66.4410192
	84.4040621	-66.4572873
0538-69.1	84.4594787	-69.1853297
	84.4419024	-69.1807092
	84.4559968	-69.1749655
	84.4334023	-69.1766826
	84.4540144	-69.1701029
0540-69.7	85.01919	-69.7437424
0540-69.3	85.0469401	-69.3316404
0543-68.9	85.719722	-68.9449483

Table 2: WISE-detected YSO candidates associated with SNRs in the LMC. Object numbers (Column 1) refer to those SNR in our source catalog (Table 2) found to have YSOs within a $10'$ radius. The positions for the YSOs (Columns 2, 3) are taken directly from the WISE Point-Source Catalog.